Going Unconstrained with Rolling Shutter Deblurring
(Supplementary Material)

Mahesh Mohan M. R., A. N. Rajagopalan
Indian Institute of Technology Madras
{ee14d023,raju}@ee.iitm.ac.in

Gunasekaran Seetharaman
U.S. Naval Research Laboratory
guna.seetharaman@nrl.navy.mil

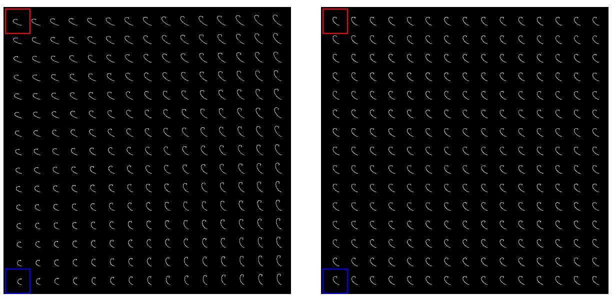

(a) With inplane rotations (b) *Without* inplane rotations

Figure S1. Full set of PSFs of Fig. 2(b) illustrating the effect of inplane rotations for wide-angle setting (29 mm) using [6].

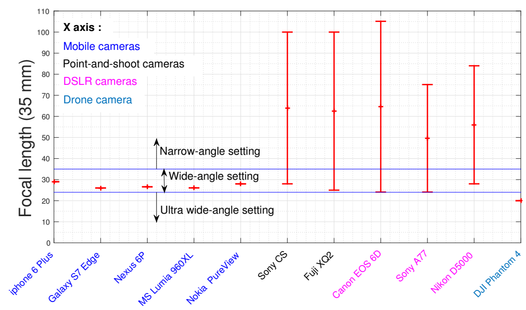

Figure S2. Focal lengths of some popular CMOS devices. Note the wide-angle setting predominant in cell-phone and drone cameras.

We begin by revisiting the problem motivation. This is followed by section S2 which contains our proof for claim 2 (section 3). Section S3 gives implementation details, and section S4 is devoted to additional evaluations.

S1. Problem Motivation (illustrative)

As mentioned in section 1 in the main paper, our method advances the state-of-the-art in RS deblurring, as it can deal with wide-angle configuration, unconstrained ego-motion and unconstrained shutter, *without* the need for timing information. Here, we further elaborate the significance of these problems that we have addressed in our work.

Unconstrained Focal-length: The PSFs provided in Fig. 2(b), which illustrates the importance of inplane rotations for wide-angle systems, is created using a focal length of 29 mm and real hand-held trajectory #39 in [6]. The full set of PSFs is provided in Fig. S1. We give in Fig. S2 focal-length settings of some popular CMOS imaging devices. It is clearly evident from the figure that wide-angle configurations are indeed important in photography (and predominant in cell-phones and drone cameras). However, the state-of-the-art RS-BMD [11] works only for narrow-angle settings. Hence, it is important to accommodate wide-angle settings.

Unconstrained Ego-motion: Even though a polynomial function can reasonably model human camera shake, RS blur also exists in images captured by drones, street view cars, *etc*., wherein the ego-motion is seldom regular [11]. Fig. S3 illustrates this fact with an under-damped response of a robotic system (which we employed in Figs. 5(d-f) using [4]). Also given is the approximation using a fourth order polynomial (as used in state-of-the-art RS-BMD [11]). From the plot it is clear that the polynomial model is *unable* to adequately capture the motion, thus underscoring the need for handling unconstrained ego-motion.

RS timing information: Both shutter speed (t_e) and inter-row delay (t_r) are required a priori in state-of-the-art RS-BMD [11] to fragment the motion trajectory for each image-row. Getting t_r from a camera requires processing of videos taken using the same camera setting (section 5.2 in [11]). Deriving both t_e and t_r *without* the meta-data and camera information further escalates the difficulty. In contrast, our method does *not* need any a priori timing information. Note that we estimate the value t_r/t_e for the RS prior in Eq. (9) solely from image intensities as discussed in section 4.4.

S2. Proof of Claim 2

Claim 2: *The prior which restricts drifting of TSFs between blocks (in Eq.* (9)*) is a convex function in* $\mathbf{w}$*, and can be represented as a norm of matrix vector multiplication,* i.e., *as* $\|\mathbf{G}\mathbf{w}\|_2^2$*, with sparse* $\mathbf{G}$.

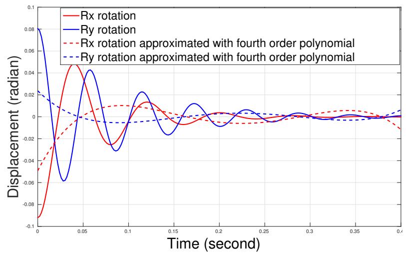

Figure S3. Vibrational ego-motion of a robotic system (using [4]). The polynomial model is *inadequate* to capture these trajectories.

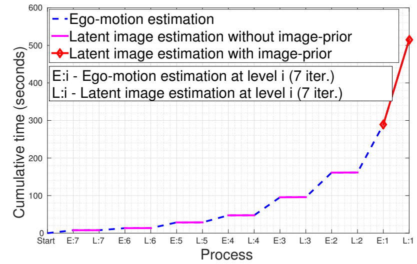

Figure S4. Cumulative time for different processes. Note the computational gains of the prior-less RS-EFF based image estimation.

To prove this, we draw from the following well-known properties of convex function [1] which are a linear function is always convex (prop. 1), composition of convex functions is always convex (prop. 2), and non-negative sum of convex functions is convex (prop. 3).

Proof: Considering n_b number of image blocks and each block-MDF $w_\mathbf{i}$ having length l, an individual additive component in our RS prior (in Eq. (9)) can be represented as $\|\Gamma\left(r_b(\mathbf{j}-\mathbf{i}+1)\right)\cdot \mathbf{S}_{(\mathbf{i},\mathbf{j})}\mathbf{w}\|_2^2$, where $\mathbf{S}_{(\mathbf{i},\mathbf{j})}$ is a matrix of dimension $l \times n_b \cdot l$, with all zeros except two scaled identity matrices of dimension $l \times l$ corresponding to $\mathbf{i}$th TSF (with scale 1) and $\mathbf{j}$th TSF (with scale -1). Therefore, the term $\{\Gamma\left(r_b(\mathbf{j}-\mathbf{i}+1)\right)\cdot \mathbf{S}_{(\mathbf{i},\mathbf{j})}\mathbf{w}\}$ is a linear function in $\mathbf{w}$. Since $\|\Gamma\left(r_b(\mathbf{j}-\mathbf{i}+1)\right)\cdot \mathbf{S}_{(\mathbf{i},\mathbf{j})}\mathbf{w}\|_2^2$ is a composite of squared L_2 norm (which is convex) of a linear function in $\mathbf{w}$, each additive component is convex (props. 1 and 2). Resultantly, the sum of all additive components in Eq. (9), *i.e.*, prior($\mathbf{w}$), is a convex function in $\mathbf{w}$ (prop. 3).

Also, prior($\mathbf{w}$) can be represented as $\|\mathbf{G}\mathbf{w}\|_2^2$, where matrix $\mathbf{G}$ is obtained by vertically concatenating matrices $\{\Gamma\left(r_b(\mathbf{j}-\mathbf{i}+1)\right)\cdot \mathbf{S}_{(\mathbf{i},\mathbf{j})}\}$ corresponding to the individual additive component in RS prior. Since $\mathbf{S}_{(\mathbf{i},\mathbf{j})}$ is a sparse matrix, $\mathbf{G}$ will also be sparse. Hence proved. ∎

S3. Implementation Details

We implemented our algorithm in `MATLAB`. We empirically set 7 scales, each with 7 iterations, in our scale-space framework (section 4). The blurred image in the ith scale is formed by downscaling the input image by a factor of $(1/\sqrt{2})^{i-1}$. To start the alternative minimization, the coarsest scale MDFs are initialized with Kronecker delta. For ego-motion estimation (section 4.2), we consistently used the RS-prior regularization (α in Eq. (13)) in level i as 2^{7-i} (so that the RS prior can cope with the increasing image size, and thus the data fidelity magnitude $\|\mathbf{F}\mathbf{w}-\nabla\mathbf{B}\|_2^2$, in finer levels). We used the MDF regularization β' (in Eq. (13)) as 0.01. For latent image estimation (section 4.3), we used $R = 48$ such that each image-patch is square, and with 6 patches along the shorter dimension and 8 along the longer dimension. For the Richardson-Lucy deconvolution (employed in the last iteration of the finest level), we used a total number of 30 iterations. For the selection of block-size (section 4.4), we used an initial block-size r_0 as 145, and a downscaling factor of 2 (*i.e.*, $M_0 = M/2$ and $N_0 = N/2$).

Running time reported in Table 1 is obtained on the same system with an Intel Xeon processor with 32 GB memory. We found that for deblurring an 800×800 RGB image (of maximum blur-length of 30 pixels), our unoptimized `MATLAB` implementation took about 9 minutes. Fig. S4 provides a detailed break-up of the time taken for each estimation step. In fact, observe that a large fraction of the total time is utilized for latent image estimation in the *final* iteration which involves a costly image-prior (see section 4.3). This underscores the importance of our efficient prior-less estimation in the initial iterations derived from RS-EFF (Eq. (14)).

S4. Additional Evaluations

We provide in Fig. S5 iteration-by-iteration results to illustrate how the algorithm works. In Fig. S6, we give full images corresponding to the patches of synthetic experiment results provided in Figs. 5(a-i). In Figs. S7-S11, we give additional evaluations for the real RS-BMD examples provided in Figs. 7 & 8. These include SIV-BMD [2] and RS rectification followed with SIV-BMD [2] (as reported in [11]), and state-of-the-art CCD-BMD [9]. We also consider BMD *without* our RS prior to illustrate the ego-motion ambiguity in RS-BMD. For low-light case, we consider [5] that specifically addresses low-light BMD (albeit for CCD cameras). The codes for [5], [11] and [9] are downloaded from the author's website and executed using default parameters. Additional examples under different lighting condition and for wide-angle settings are given in Fig. S12.

For sake of completeness; we provide GS deblurring comparisons with state-of-the-art CCD-BMD methods of [9, 8, 10, 13, 12] and [3] in Figs. S13 & S14. We evaluated on the examples from the dataset of [7] and [9] using their reported results. The results show that our method works equally well for CCD cameras and importantly, *without* warranting any prior knowledge of the shutter.

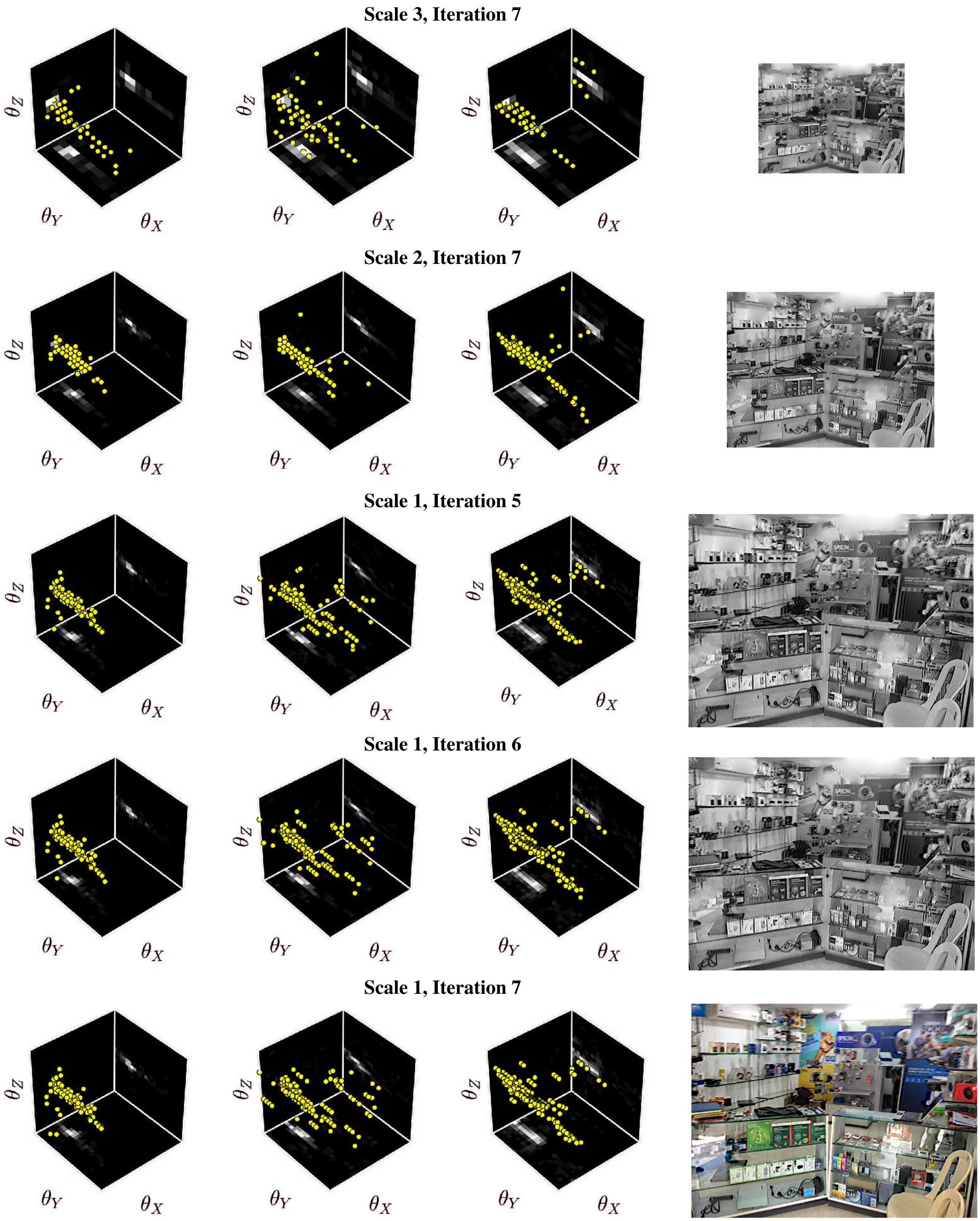

(a) MDF 1 ($\mathbf{w_1}$) (b) MDF 2 ($\mathbf{w_2}$) (c) MDF 3 ($\mathbf{w_3}$) (d) Latent image ($\mathbf{L}$)

Figure S5. Iteration-by-iteration results of the alternative minimization of block-wise MDFs and latent image: (a-c) Estimated block-wise MDFs and (d) Estimated latent image. Notice the variation in block-wise MDFs, which depicts the characteristic of RS blur (as shown in Fig. 3). Also, observe the convergence of the block-wise MDFs through iteration 5 to 7 in the finest image scale (last three rows).

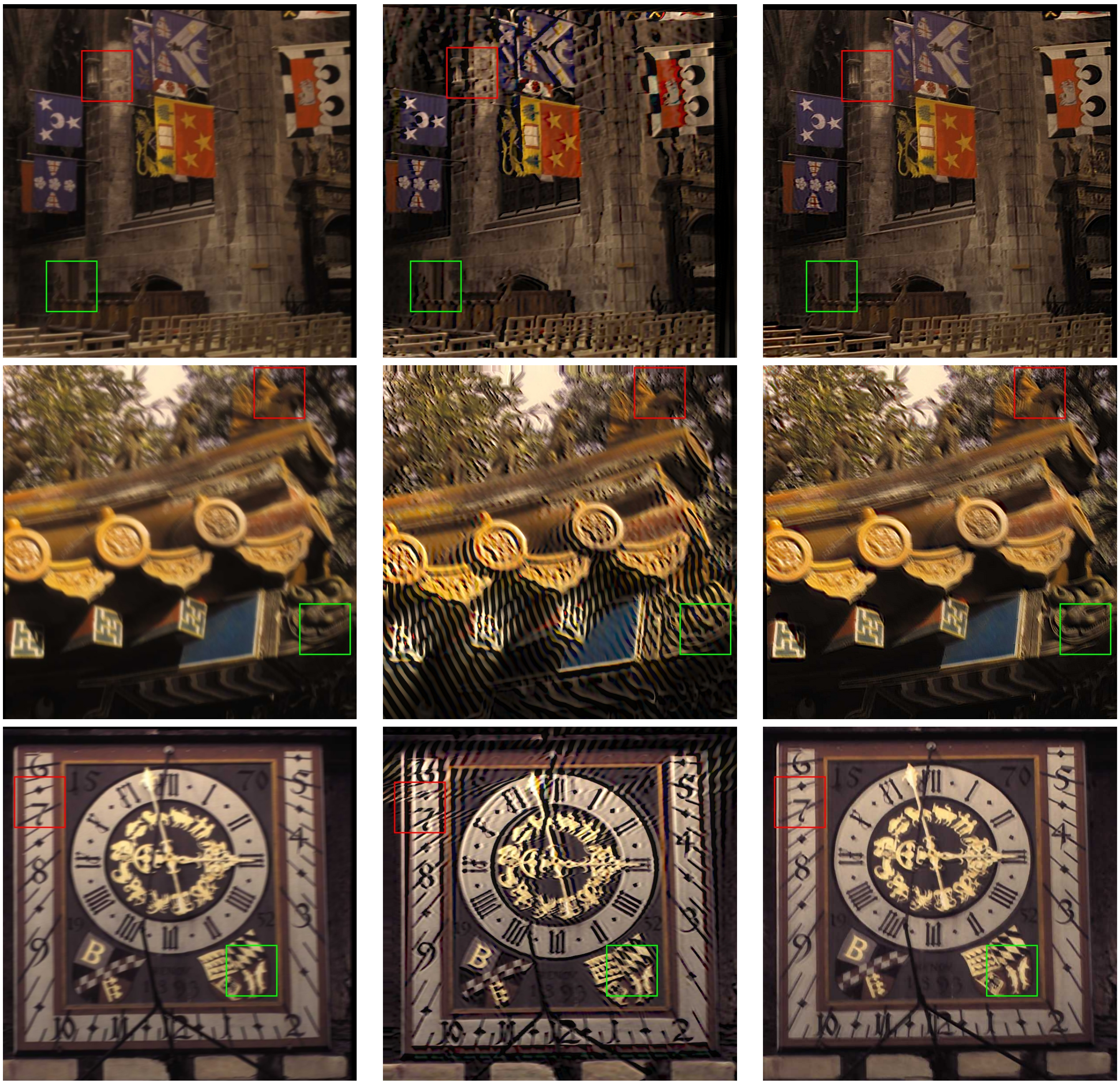

(a) Input (b) Su and Heidrich [11] (c) Ours

Figure S6. Full-sized images corresponding to the image patches given in Figs. 2(a-i): First row gives a case of wide-angle system (Figs. 2(a-c)), second row gives a case of vibratory motion (Figs. 2(d-f)), and third row gives a case of CCD-blur (Figs. 2(g-i)). (Best viewed on high-resolution display with zoom-in corresponding to an 800×800 image size.)

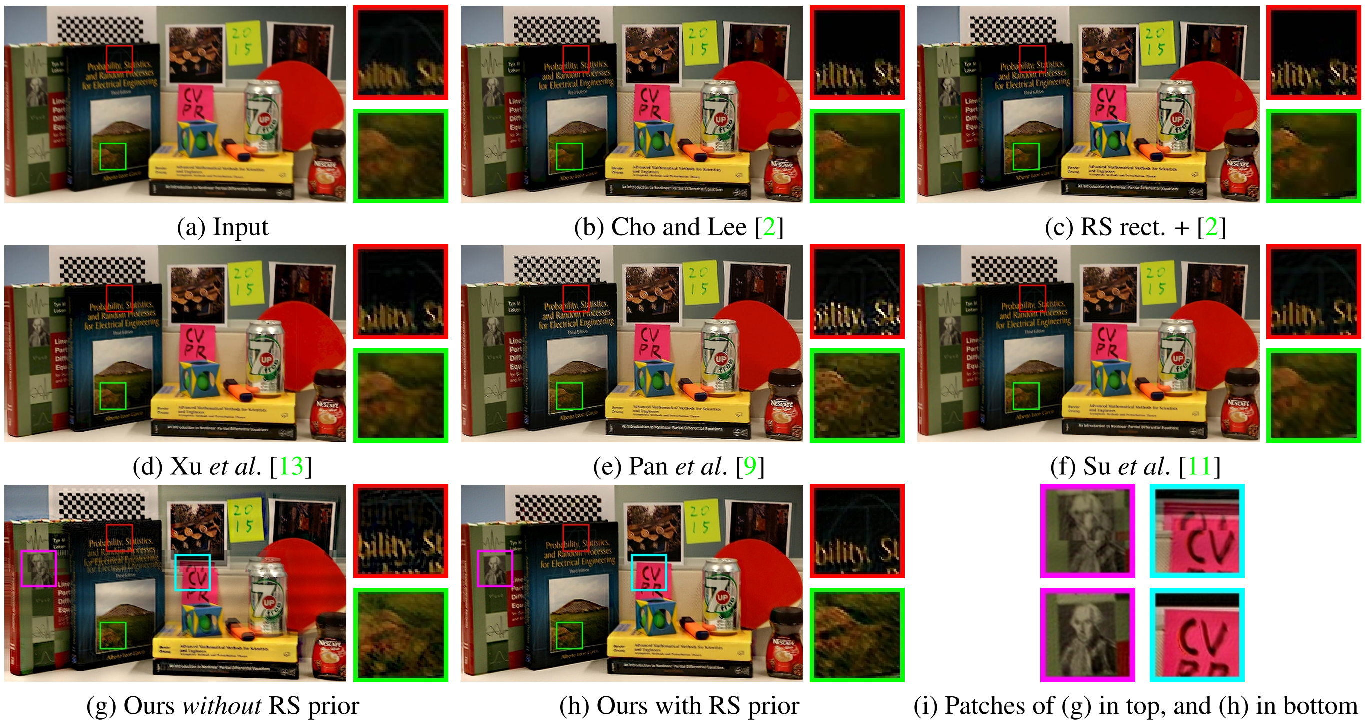

Figure S7. Detailed comparisons for RS narrow-angle example in dataset [11] (Fig. 7-top-row). Note the effect of incoherent combination due to the block shift-ambiguity (section 3, claim 1) in (i)-first row, which is successfully suppressed by our RS prior ((i)-second row).

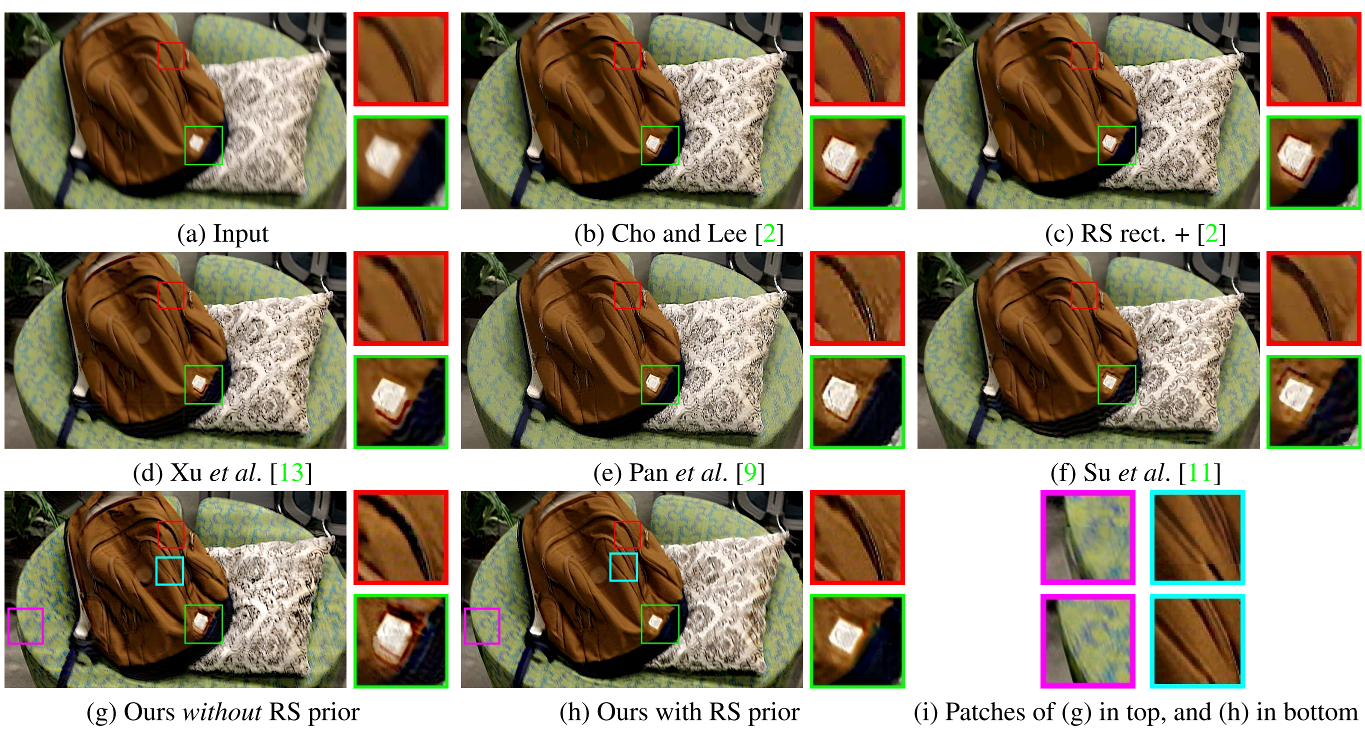

Figure S8. Detailed comparisons for RS narrow-angle example in dataset [11] (Fig. 7-second-row). Our method recovers finer details (see bag-zipper in patch 1), and deblur with negligible ringing artefacts (see bag-badge in patch 2), as compared to competing methods.

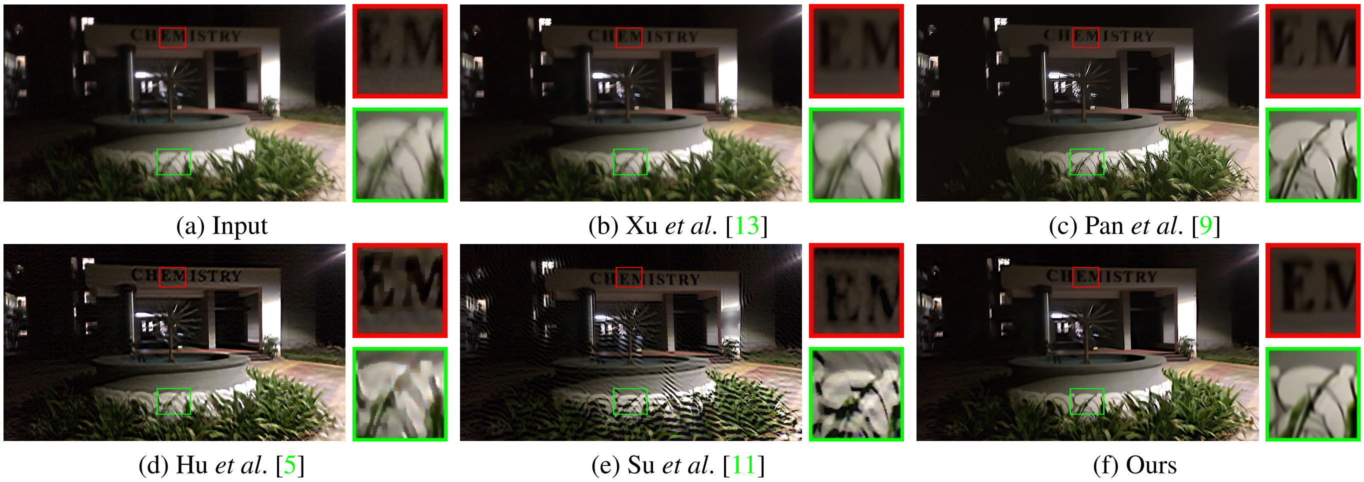

Figure S9. Detailed comparisons for RS wide-angle example (Fig. 8-first row). In contrast to competing methods, our method models the RS ego-motion better (observe the residual blur in the letters, and the repeated occurrence of the longest grass leaf in (c)).

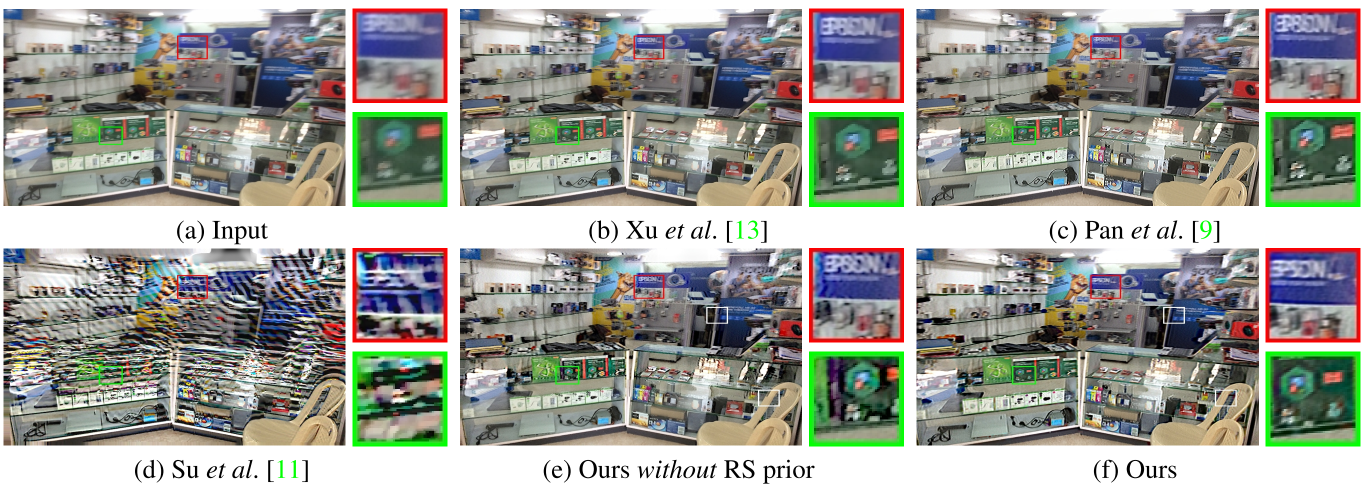

Figure S10. Comparisons for RS wide-angle case (Fig. 8-second row). White boxes in images (e) and (f) show the effect of RS prior.

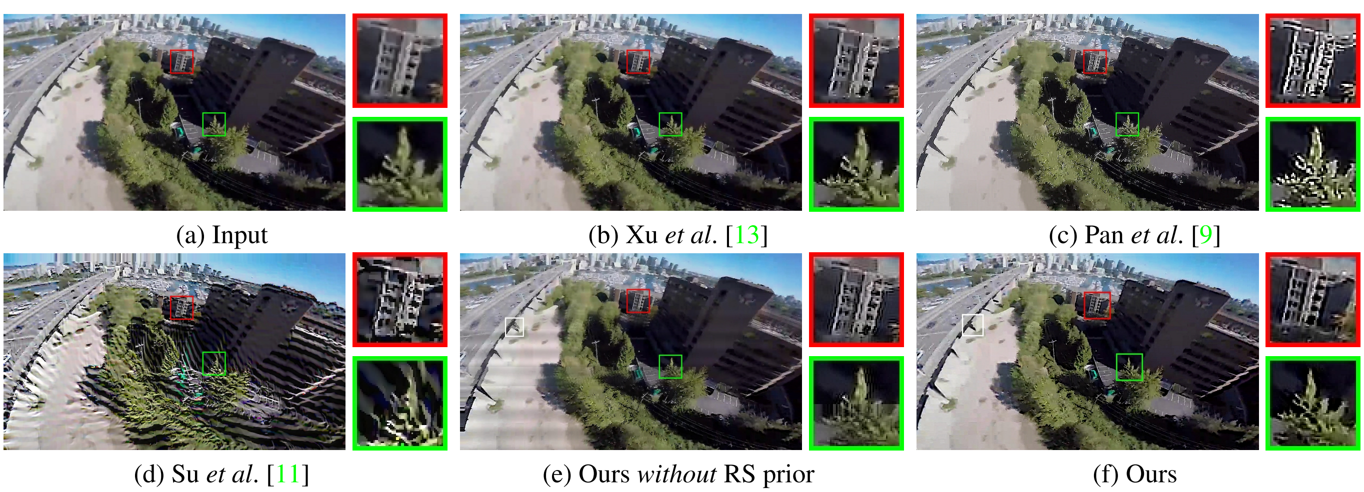

Figure S11. Comparisons for RS wide-angle example (Fig. 8-third row). White box in images (e) and (f) shows the effect of RS prior.

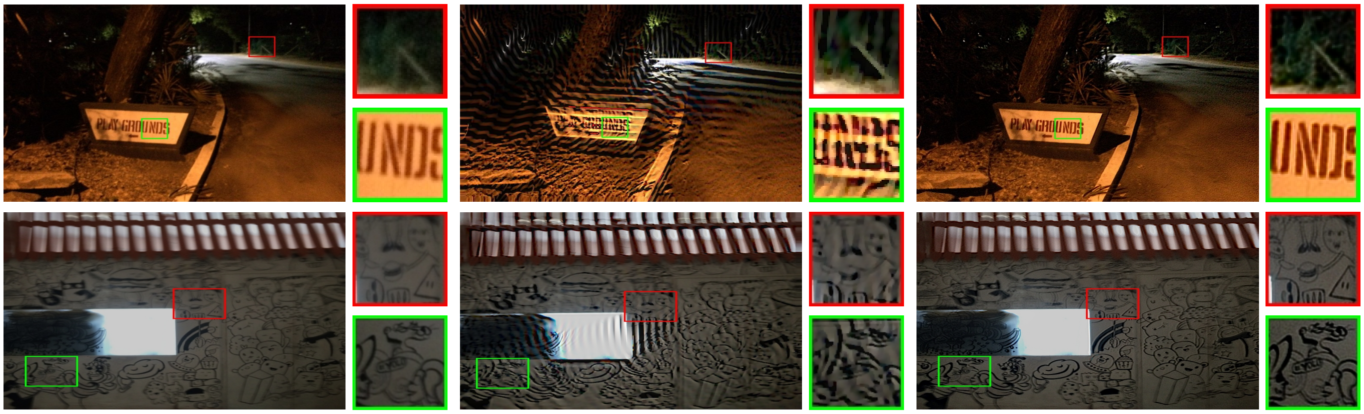

(a) Input (b) Su *et al*. [11] (c) Ours

Figure S12. Additional RS comparisons with state-of-the-art RS-BMD method [11] under different lighting conditions and for wide-angle settings. Note the inefficacy of the competing method in dealing with wide angle systems.

(a) Input (b) Michaeli *et al*. [8] (c) Perrone *et al*. [10]

(d) Xu *et al*. [13] (e) Pan *et al*. [9] (f) Ours

Figure S13. Comparisons for CCD blur example in dataset [7]. Our result is comparable with [8, 10, 13] and [9].

(a) Input (b) Gupta *et al*. [3] (c) Whyte *et al*. [12]

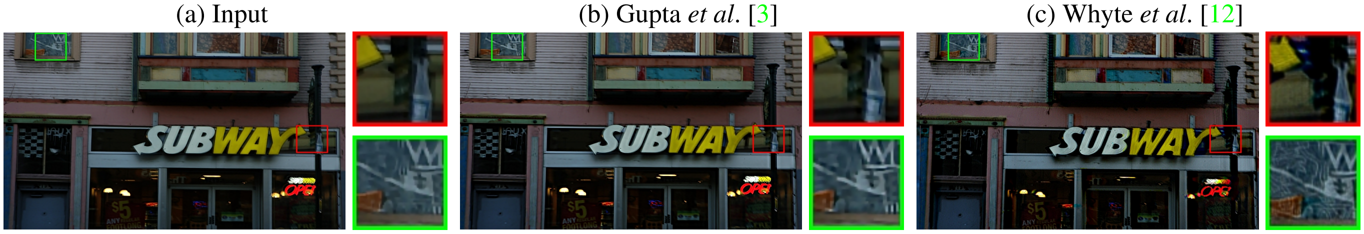

(d) Xu *et al*. [13] (e) Pan *et al*. [9] (f) Ours

Figure S14. Comparisons for CCD blur example in dataset [9]. Our result is comparable with [3, 12, 13] and [9].

References

[1] S. Boyd and L. Vandenberghe. *Convex optimization*. Cambridge university press, 2004. 2

[2] S. Cho and S. Lee. Fast motion deblurring. In *ACM Transactions on Graphics (TOG)*, volume 28, page 145. ACM, 2009. 2, 5

[3] A. Gupta, N. Joshi, C. L. Zitnick, M. Cohen, and B. Curless. Single image deblurring using motion density functions. In *European Conference on Computer Vision (ECCV)*, pages 171–184. Springer, 2010. 2, 7

[4] M. R. Hatch. *Vibration simulation using MATLAB and ANSYS*. CRC Press, 2000. 1, 2

[5] Z. Hu, S. Cho, J. Wang, and M.-H. Yang. Deblurring low-light images with light streaks. In *IEEE Conference on Computer Vision and Pattern Recognition (CVPR)*, pages 3382–3389, 2014. 2, 6

[6] R. Köhler, M. Hirsch, B. Mohler, B. Schölkopf, and S. Harmeling. Recording and playback of camera shake: Benchmarking blind deconvolution with a real-world database. In *European Conference on Computer Vision (ECCV)*, pages 27–40. Springer, 2012. 1

[7] W.-S. Lai, J.-B. Huang, Z. Hu, N. Ahuja, and M.-H. Yang. A comparative study for single image blind deblurring. In *IEEE Conference on Computer Vision and Pattern Recognition (CVPR)*, pages 1701–1709. IEEE, 2016. 2, 7

[8] T. Michaeli and M. Irani. Blind deblurring using internal patch recurrence. In *European Conference on Computer Vision (ECCV)*, pages 783–798. Springer, 2014. 2, 7

[9] J. Pan, D. Sun, H. Pfister, and M.-H. Yang. Blind image deblurring using dark channel prior. In *IEEE Conference on Computer Vision and Pattern Recognition (CVPR)*, pages 1628–1636. IEEE, 2016. 2, 5, 6, 7

[10] D. Perrone and P. Favaro. Total variation blind deconvolution: The devil is in the details. In *IEEE Conference on Computer Vision and Pattern Recognition (CVPR)*, pages 2909–2916. IEEE, 2014. 2, 7

[11] S. Su and W. Heidrich. Rolling shutter motion deblurring. In *IEEE Conference on Computer Vision and Pattern Recognition (CVPR)*, pages 1529–1537. IEEE, 2015. 1, 2, 4, 5, 6, 7

[12] O. Whyte, J. Sivic, A. Zisserman, and J. Ponce. Non-uniform deblurring for shaken images. *International journal of computer vision (IJCV)*, 98(2):168–186, 2012. 2, 7

[13] L. Xu, S. Zheng, and J. Jia. Unnatural l0 sparse representation for natural image deblurring. In *IEEE Conference on Computer Vision and Pattern Recognition (CVPR)*, pages 1107–1114. IEEE, 2013. 2, 5, 6, 7